Electronic Supplementary Information - Phys. Chem. Chem. Phys.

Spectro-microscopic photoemission evidence of surface dissociation and charge uncompensated areas in $Pb(Zr,Ti)O_3(001)$ layers

Dana Georgeta Popescu[a], Marius Adrian Huşanu[a], Lucian Trupină[a], Luminiţa Hrib[a], Lucian Pitilie[a], Alexey Barinov[b], Silvano Lizzit[b], Paolo Lacovig[b], and Cristian Mihail Teodorescu[a*]

[a]National Institute of Materials Physics, Atomistilor 105b, 077125 Măgurele-Ilfov, Romania.
[b]Elettra Sincrotrone Trieste, S.S. 14 - km 163,5, Area Science Park, 34169 Basovizza-Trieste, Italy.

[*]Corresponding Author, e-mail: teodorescu@infim.ro

1. Structure of PZT(001) layers

1.1. Low energy electron diffraction (LEED) pattern of a 10 nm PZT(001) layer after annealing at 400 °C for three hours in 5 x 10^{-5} mbar oxygen pressure (kinetic energy: 73 eV). (1 x 1) patterns are visible.

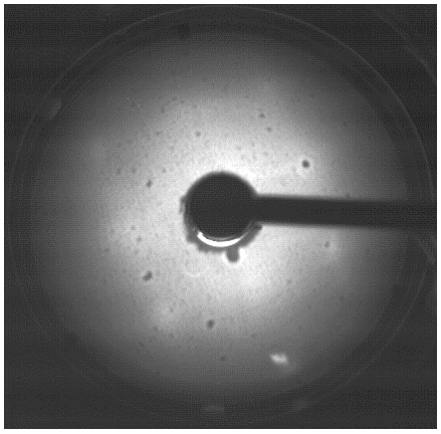
(a)

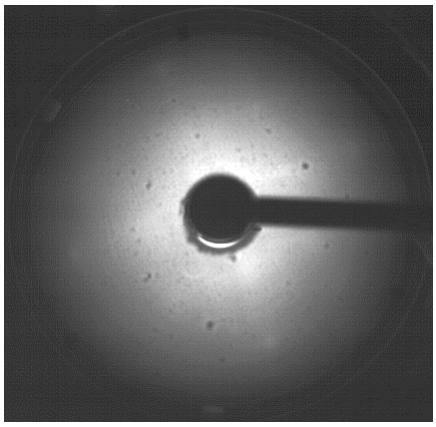
(b)

Figure ESI-1. LEED on a 10 nm PZT/SRO/STO(001) thin film, after the cleaning procedure in O_2, recorded with electron kinetic energies of (a) 73 eV; (b) 100 eV.

1.2. X-ray photoelectron diffraction data (polar scans) obtained on a 250 nm PZT(001) layer after the annealing procedure

Figure 2(a) presents an ideal structure of a stack of two PZT elementary cells along the direction [001], with the main angles where forward focusing maxima could be observed. For the theory of X-ray photoelectron diffraction (XPD), see e.g. Ref. [ESI-1]. The values in parantheses correspond to the cubic structure ($a = c$). Figure 2(b, c) represent Pb 5d XPS data taken with 74 eV photon energy at different polar angles along the [100] and [110] directions. These spectra are integrated, a parabolic background is subtracted and yield the asymmetry patterns represented in Fig. 2(d). It might be seen that a clear asymmetry is observed in the polar scan along the [100] direction, whereas the XPD signal along the [110] direction presents lower asymmetry. In order to explain this, one has to notice: (a) this experiment is not exactly an X-ray photoelectron diffraction experiment where the forward focusing formalism may be applied, since here the kinetic energy of the photoelectrons is rather low; rather, a multiple scattering approach must be employed; (b) along the [110] direction, forward focusing maxima should appear also at 25.2° and 19.5° apart from the 35.3° peak, and all these signals are probably mixed together.

Based on these data, an attempt of deriving the *c*/*a* ratio can be made, and the results obtained are 1.26 for the maximum at 21.6°, 1.04 for the maximum at 43.9°, and 1.11 for the maximum at 32.5°. From the X-ray diffraction (XRD) data [ESI-2] the substrate (STO) lattice parameter yields 3.90 ± 0.03 Å, whereas the *c* parameter of a PZT film grown in similar conditions yields 4.1325 ± 0.025 Å from the (001) and (002) peaks of PZT, therefore *c*/*a* = 1.060 ± 0.002. However, by taking into account that the cubic PZT has a lattice parameter of 4.05 Å [ESI-3] and assuming that the volume of the PZT elementary cell is roughly the same between the cubic and the tetragonal phase, *c*/*a* should result such as the ratio of the cubed lattice parameters of PZT and STO, yielding around 1.12. The average of the values derived by XPD is 1.137, which is not far away from the above assumption. The discrepancy between the value obtained by XPD and the value reported by XRD could also be connected to the different probing depths of the two techniques: practically, the whole layer for XRD and just the outermost 2-3 elementary cells by the actual XPD data, owing to the low inelastic mean free path of the detected electrons (4-6 Å). Also, the two layers, despite being prepared in similar conditions, have a different history: the XRD data are recorded under air, whereas the XPD data are recorded in ultrahigh vacuum, after cleaning in oxygen atmosphere. The samples under air, owing to the adsorption of contaminants, may loose their polarization [ESI-4] and could even promote the creation of some vacancies or other kind of defects yielding the 'compression' of the average elementary cell. Therefore, the fact that the tetragonal distortion obtained for the outermost layers in PZT(001) after the UHV cleaning procedure is about the double of the sample investigated under air may be explained by several mechanisms.

The main conclusion of these XPD data is that the thick (250 nm) samples present crystalline order at their surface, even though the LEED patterns were not visible.

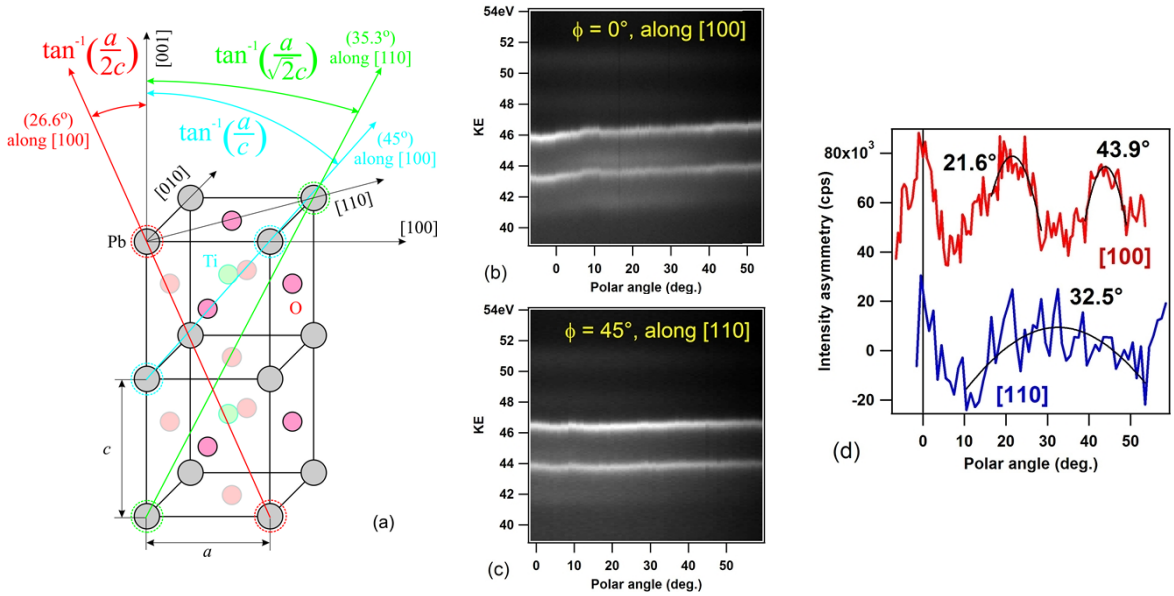

Figure ESI-2. X-ray photoelectron diffraction from Pb 5d core levels: (a) principle to identify the main directions of forward focusing; (b,c) the XPS spectra recorded at different polar angles, over two azimuths; (d) the XPD signal detected after integrating the XPS spectra and subtracting a smooth background.

2. X-ray photoelectron spectroscopy

2.1. Complete evolution of XPS spectra for PZT(001): Pb 4f (a), Zr 3d (b), Ti 2p (c), O 1s (d) over several hours of measurement. For each series, the first and the last spectrum are plotted in the corresponding panels Fig. 3, main text.

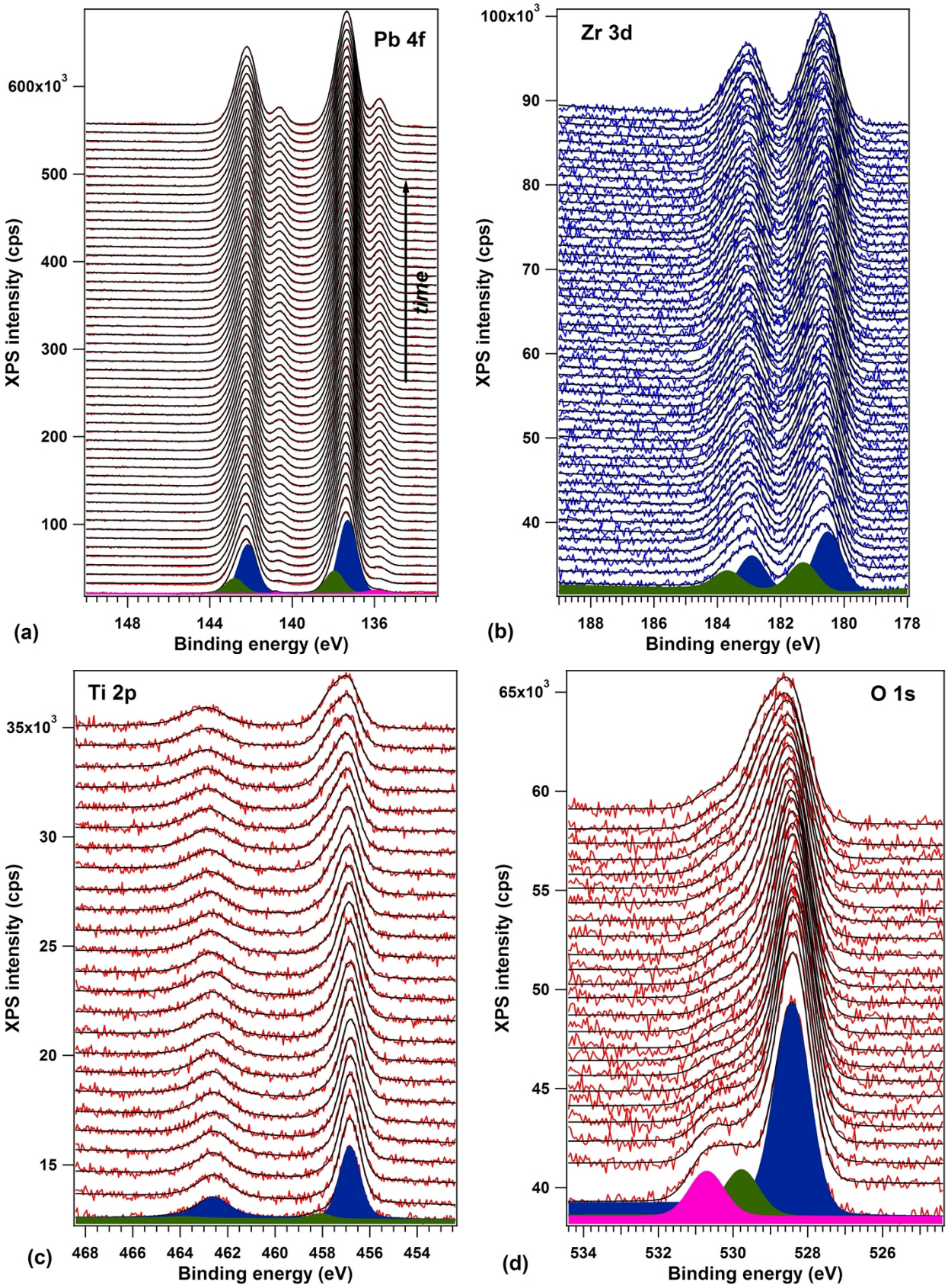

2.2. Time dependence of binding energies of separate components resulted from the analysis presented in Figure 3 (main text) for a $Pb(Zr,Ti)O_3(001)$ of 20 nm thickness. The binding energies are approximately constant. Their absolute values of binding energies are of about 0.5 ± 0.2 eV

lower than the values reported in Ref. [ESI-5], which is reasonable, given the fact that there was no flood gun used in the synchrotron radiation experiment.

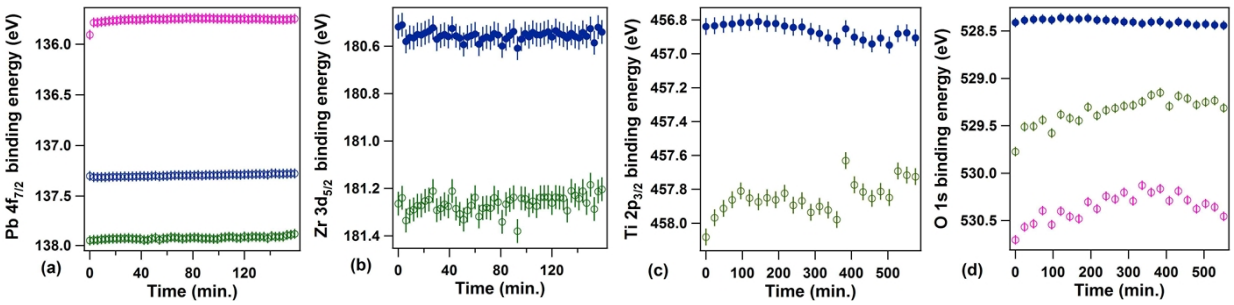

Figure ESI-4. Evolution of binding energies for the different components resulted from the deconvolution of XPS spectra of a 20 nm PZT(001) sample: (a) Pb $4f_{7/2}$; (b) Zr $3d_{5/2}$; (c) Ti $2p_{1/2}$; (d) O 1s.

2.3. Inelastic mean free path effects in the derivation of sample stoichiometry

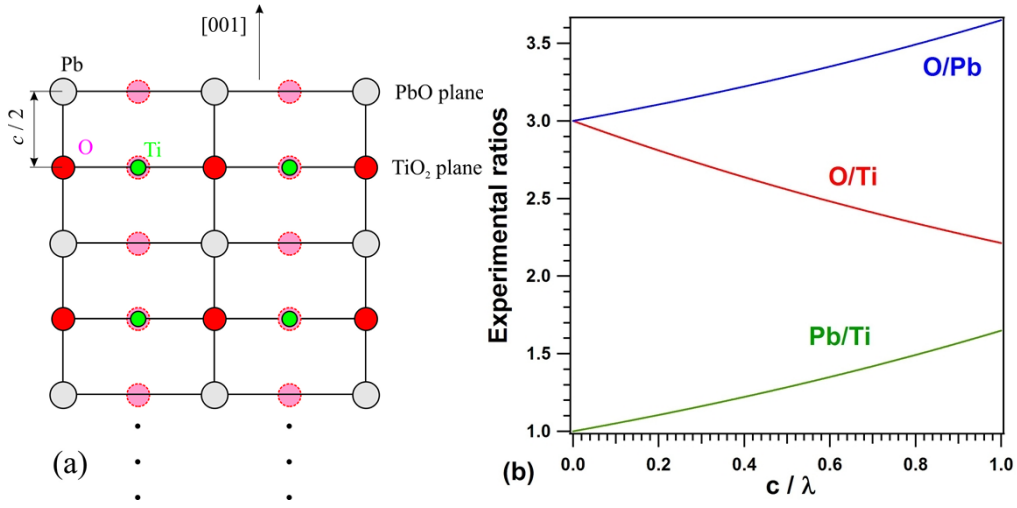

Figure ESI-5: (a) side view of a (001) $PbTiO_3$ layer, evidencing PbO and TiO_2 layers; (b) Experimental ratio between Pb and Ti, O and Ti, and O and Pb concentrations, by taking into account inelastic mean free paths effects illustrated by equations (ESI-1)-(ESI-3).

For an elementary cell of the perovskite $PbTiO_3$ structure represented in Fig. ESI-5(a), by taking into account electron inelastic mean free paths (IMFP) effects, and assuming that the IMFP (λ) is roughly the same for all core levels analyzed (the corresponding kinetic energies are around 162 eV for Pb 4f, 119 eV for Zr 3d, 143 eV for Ti 2p, and 72 eV for O 1s), the number of atoms detected by XPS will be expressed as:

$$N(\mathrm{Ti}) = \exp\left(-\frac{c}{2\lambda}\right) + \exp\left(-\frac{3c}{2\lambda}\right) + \exp\left(-\frac{5c}{2\lambda}\right) + \ldots \qquad \text{(ESI-1)}$$

(The same holds also for Zr.)

$$N(\mathrm{Pb}) = 1 + \exp\left(-\frac{c}{\lambda}\right) + \exp\left(-\frac{2c}{\lambda}\right) + \ldots \qquad \text{(ESI-2)}$$

$$N(\mathrm{O}) = 1 + 2\exp\left(-\frac{c}{2\lambda}\right) + \exp\left(-\frac{c}{\lambda}\right) + 2\exp\left(-\frac{3c}{2\lambda}\right) + \exp\left(-\frac{2c}{\lambda}\right) + \ldots \qquad \text{(ESI-3)}$$

The dependence of obtained concentration ratios on the ratio between the lattice parameter along [001] (c) and the IMFP are represented in Fig. ESI-5(b).

2.4. Evolution with time of the stoichiometry of the 20 nm PZT(001) layer

From the amplitudes represented in Fig. 4 (main text), one applies the atomic photoionization cross sections [ESI-6] and normalizes by the flux on the sample (a factor of 1.72 between the flux at 300 eV and that at 600 eV on SuperESCA), together with a factor of 3 in the beam intensity between the Pb 4f + Zr 3d experiment and the (Ti 2p + O 1s) one due to a disallignment of the beamline between these experiments. A Pb/(Ti+Zr) ratio of about 1.5 is obtained for the first series of spectra. Thus, one uses the fact that for all series of samples investigated by laboratory XPS, the Pb/(Zr + Ti) ratio was close to 1, see Refs. 3, 4, 18 from the main text. From here, one derives the ratio $c/\lambda \approx 0.7$-0.8 then the IMFP yields 5.3-6.2 Å, in good agreement with the 'universal curve' known for electron spectroscopy (Ref. 26, main text). Furthermore, the O 1s signal is re-calibrated by taking into account that the detection efficiency of the Phoibos analyzer is about 1.4 times larger for low energy electrons (about 70 eV kinetic energy) than for the other signals, at about 120-160 eV.

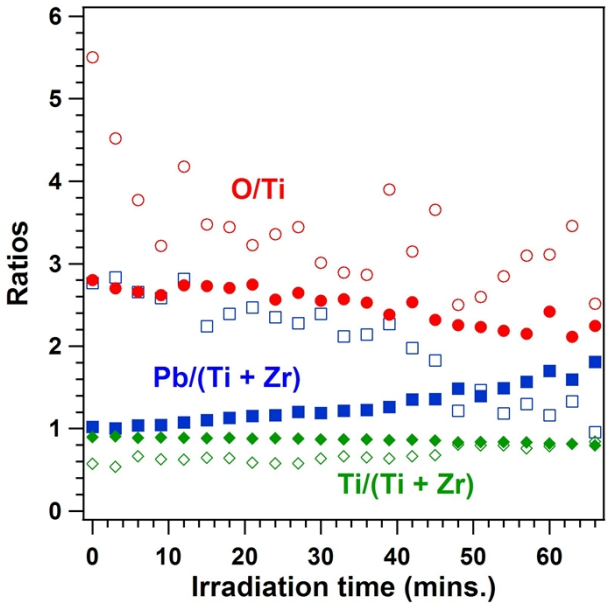

Figure ESI-6. The variations in time of relevant atomic concentration ratios, separated between the $P^{(+)}$ component (lower binding energy, full symbols) and the $P^{(++)}$ component (higher binding energy, empty symbols). There is a clear Pb enrichment and oxygen depletion of the main component.

The stoichiometry is computed by considering separately the 'main' components for all signals, which are attributed to the $P^{(+)}$ state, and the components shifted towards higher binding energy, by about 0.7-0.9 eV (see Fig. ESI-4). These components are attributed to the $P^{(++)}$ state, see the main text for more comments. The results are represented in Fig. ESI-6.

The composition evolution yields as follows:

- for the $P^{(+)}$ component: $Pb_{1.02}Ti_{0.90}Zr_{0.10}O_{2.80} \rightarrow Pb_{1.81}Ti_{0.80}Zr_{0.20}O_{2.24}$;
- for the $P^{(++)}$ component: $Pb_{2.76}Ti_{0.57}Zr_{0.43}O_{5.50}$ ($\approx$ 1.76 PbO + $PbTi_{0.57}Zr_{0.43}O_{2.74}$) $\rightarrow$ $Pb_{0.95}Ti_{0.84}Zr_{0.16}O_{2.52}$.

PbO, in fact, has a similar binding energy as metal Pb [ESI-7], but in this case this PbO is formed on $P^{(++)}$ areas and might be shifted towards higher binding energies, as does the C 1s from the inherent contamination [ESI-4].

Let us recall that these are surface compositions, valid at most within a depth of $3\lambda \approx 18$ Å $\approx$ 9 atomic layers.

Two general remarks are the following: (i) with irradiation, the oxygen content of both components decreases; (ii) with irradiation, the surface Pb content of the $P^{(++)}$ component increases considerably.

References:

[ESI-1] A. Pancotti, J. Wang, P. Chen, L. Tortech, C.M. Teodorescu, E. Frantzeskakis, and N. Barrett, *Phys. Rev. B*, 2013, **87**, 184116.
[ESI-2] L.E. Stoflea, N.G. Apostol, C. Chirila, L. Trupina, R. Negrea, L. Pintilie, and C.M. Teodorescu, *J. Mater. Sci.*, 2014, **49**, 3337-3351, Electronic Supplementary Material.
[ESI-3] X.J. Zheng, J.G. Li and Y.C. Zhou, *Acta Materialia*, 2004, **52**, 3313-3322.
[ESI-4] L.E. Ştoflea, N.G. Apostol, L. Trupină, and C.M. Teodorescu, 2014, *J. Mater. Chem. A*, *accepted*. DOI: 10.1039/C4TA02660H.
[ESI-5] L.E. Ştoflea, N.G. Apostol, C. Chirilă, L. Trupină, R. Negrea, L. Pintilie, and C.M. Teodorescu, *J. Mater. Sci.*, 2014, **49**, 3337-3351.
[ESI-6] J.J. Yeh and I. Lindau, *Atomic Data and Nuclear Data Tables*, 1985, **32**, 1-155. See also http://ulisse.elettra.trieste.it/services/elements/WebElements.html.
[ESI-7] NIST XPS database, http://srdata.nist.gov/xps/

2.5. Evolution of Pb 4f signal for a 20 nm PZT(111) layer

A similar experiment was performed on a 20 nm PZT(111) layer. Figure ESI-7 presents the result of a three hours series of photoemission spectra on Pb 4f in similar conditions as the experiment represented in Fig. 3,(a) main text and in Fig. ESI-3(a). One clearly sees that there is no small binding energy component which develops with the sample irradiation in this case. The time-dependent chemical shift of the main line might be due to the removal of contaminants, improving the insulating character of the surface of the layer.

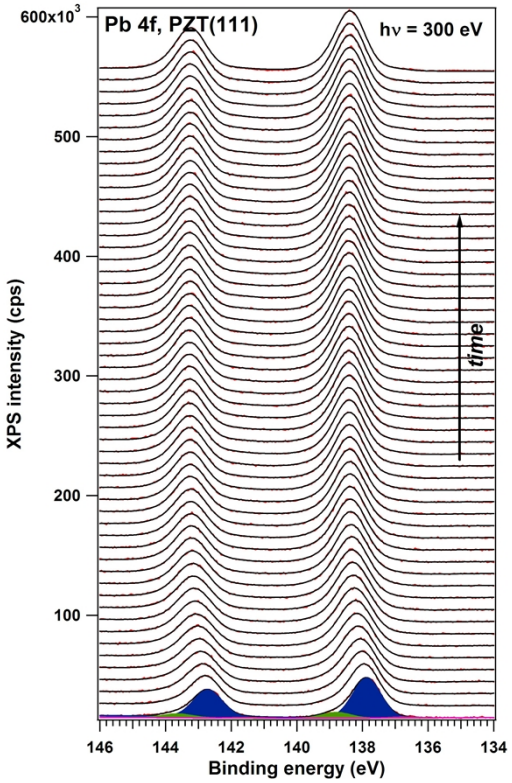

Figure ESI-7. Evolution of the Pb 4f signal with time, for a 20 nm PZT(111) layer grown on SRO/STO(111).

3. Piezoresponse force microscopy on 20 nm PZT(001) layers

Figure ESI-8 presents PFM results on the 20 nm PZT(001) layer. The amplitude and phase of the as prepared sample do not show the presence of ferroelectric domains. In order to derive the polarization imprint, a poling pattern was applied to the sample, consisting of an outer square with $P^{(+)}$ poling and an inner square with $P^{(-)}$ poling. Immediately after poling, the PFM investigation revealed some persistence of the $P^{(-)}$ area, according to Fig. ESI-8 (c) and (d). By comparing with the signals of the unpoled sample, one may affirm that the majority of the area of the as prepared sample is in the $P^{(+)}$ state, and that the stability of the $P^{(-)}$ state is within the time needed by the experiments (tens of minutes).

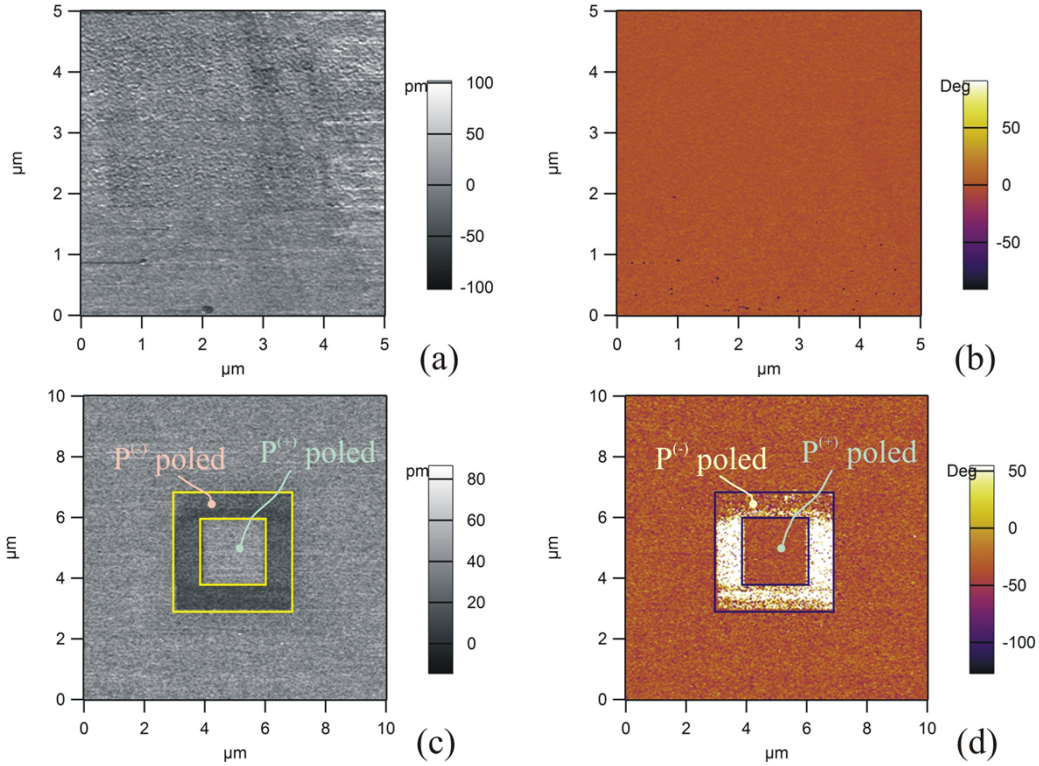

Figure ESI-8. PFM analysis of the 20 nm PZT(001) layer. As prepared sample: (a) amplitude and (b) phase. After poling the sample (10 V applied voltage on the PFM tip) with an outer area of $P^{(+)}$ poling and an inner area of $P^{(-)}$ poling: (c) amplitude; (d) phase.

4. Deconvolutions of the time resolved series of PES spectra obtained at Spectromicroscopy, and represented in Fig. 5(b)

The deconvolutions were performed with three spin orbit split doublets (Fig. ESI-9). From this analysis one may extract the time dependence of the binding energies and integral amplitudes of each component. These variations are also plotted in Fig. ESI-9(b, c, e, f). In the case of the 'light' region (Fig. ESI-9(a)), the amplitude of the low binding energy components increase with time together with a clear reduction of ther binding energies. Both the amplitude increase and the shift towards lower binding energies contribute to the fact that the low binding energy feature is progressively better resolved in the time evolution series of spectra. In the case of the 'dark' region, a similar shift towards lower binding energy of the smaller components is accompanied by a relative decrease of their intensity and an increase in the intensity of the main component, yielding less resolved small binding energy features in the total spectra. Since 'dark' regions correspond to areas with higher initial sample contamination, this analysis yields clearly the fact that progressively the contamination is removed from the sample surface, with no considerable change of the relative amplitude of the low binding energy component, which is attributed to metallic Pb.

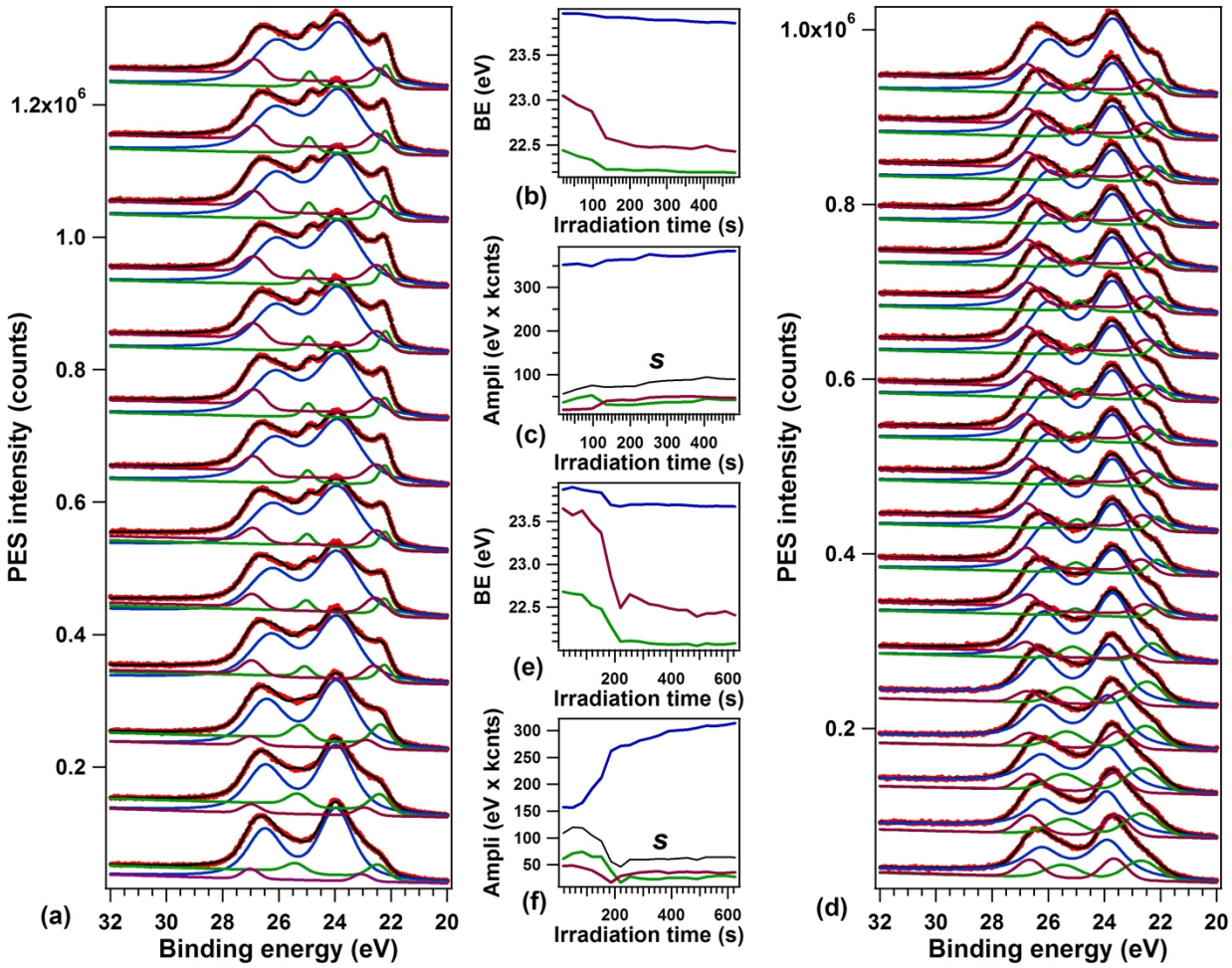

Figure ESI-9. (a) represents the time resolved series obtained in the 'light area' of Fig. 5(b), with three components whose time variation of $5d_{5/2}$ binding energies represented in (b) and that of their integral amplitudes represented in (c). (d) represents the deconvolution of the time resolved series obtained in the 'dark area' of Fig. 5(b), again with binding energies vs. time in (e) and amplitudes vs. time in (f). In (c) and (f) the black line indicated by "s" represents the sum of the green and magenta curves, i.e. the total amplitude of the low binding energy components.